Bending Properties and Lateral Resistance of Historic Timber Foundation Piles in Amsterdam, Netherlands

Hemel, Mart-Jan; Peters, Dirk Jan; Korff, Mandy

DOI
10.1061/JSENDH.STENG-13412

Publication date
2024

Document Version
Final published version

Published in
Journal of Structural Engineering (United States)

Citation (APA)
Hemel, M.-J., Peters, D. J., & Korff, M. (2024). Bending Properties and Lateral Resistance of Historic Timber Foundation Piles in Amsterdam, Netherlands. *Journal of Structural Engineering (United States)*, *151*(1), Article 04024195. https://doi.org/10.1061/JSENDH.STENG-13412

ASCE

Bending Properties and Lateral Resistance of Historic Timber Foundation Piles in Amsterdam, Netherlands

Mart-Jan Hemel, Ph.D.[1]; Dirk Jan Peters, Ph.D.[2]; and Mandy Korff, Ph.D.[3]

Abstract: Historic quay walls in many Dutch cities are supported by an array of vertical timber piles which run through soft soil deposits and rest on a sand layer, providing end-bearing support. As these structures experience horizontal loads, the foundation piles are loaded in bending. This is the dominant loading case of pile foundations of dams, lock heads, and sometimes bridge abutments as well. To accurately model and evaluate the timber pile foundations, a proper estimate of their bending properties is essential. Therefore the mechanical properties of existing spruce foundation piles, retrieved from a historic quay wall (1905) at Overamstel in Amsterdam, Netherlands, were studied. Six piles were subjected to a four-point bending experiment. The outer fiber stress was kept constant between the point loads, leading to a failure at the weakest cross section. Measurements of the curvature and force distribution were taken along the pile length during loading. In addition, biological decay in the outer layer of the timber piles, also referred to as the soft shell, was identified with microdrillings. Internal strains were measured successfully by gluing fiber-optic wires inside the soft shell of the timber piles. The experiments indicated significant variations in modulus of elasticity and modulus of rupture across the tested population, but indicated a strong correlation. Modulus of elasticity averaged 16.5 GPa with a variation coefficient of 0.30, whereas the modulus of rupture averaged 23.2 N/mm^2 with a variation coefficient of 0.26. Bacterial deterioration was found to be independent of both the outer pile diameter and the location along the timber pile. The soft shell had an average thickness of 21 mm, but it did not contribute significantly to the structural strength of the piles. This study could present a template for assessing the remaining service life not only of historic quay walls but also of other timber pile foundations under bending loads. **DOI: 10.1061/JSENDH.STENG-13412.** © *2024 American Society of Civil Engineers.*

Author keywords: Bending experiments; Timber piles; Deterioration; Microdrilling; Historic quay walls; Bending properties.

Introduction

In Amsterdam, Netherlands, during the period 1300–1600, foundations consisted of many shallow piles, named *slieten*, which relied on sleeve friction (Winsen et al. 2015). The driving of long timber piles into the first load-bearing layer of sand to support houses, bridges, and quay walls began at the end of the 16th century (Klaassen and Creemers 2012). The toe of the piles often was situated in the first sand layer at depths ranging from NAP-12 to NAP-14 m, where NAP is the standard reference for measuring elevations and depths in the Netherlands. The development of wooden pile foundations from the Middle Ages to the 20th century, based on Amsterdam's experiences, was detailed in Amsterdam Gemeente (1975). Large-scale expansion projects utilizing timber piles were already underway in the 17th and 18th centuries, eventually culminating in the late 19th and early 20th centuries, when many Dutch cities experienced substantial growth (Klaassen 2008). The timber piles mostly were made of spruce wood from Scandinavia (van Tussenbroek 2012). Alternatively, pine trees also were used, but to a lesser extent. Pile foundations used in different parts of the world have an average cap diameter of 300–500 mm, and at the toe a diameter of 120–230 mm (Das 2010). Piles in Amsterdam are smaller, with a pile cap diameter of 200–300 mm and a toe diameter of 100–150 mm. The tapering of the piles is roughly 0.005–0.01 m/m. For bridges, public buildings, and houses, timber piles mostly are loaded axially, and the loads typically are absorbed by the soil with shaft friction and toe resistance.

Historic quay walls (Fig. 1), which are the main focus of this paper, are soil-retaining structures that are used to load goods onto vessels and enable people to walk or drive on them. The soil pressure at the backside of the quay wall is increased by these service loads, causing the quay to deflect toward the canal side, accompanied by the bending of the timber piles. Therefore, quay wall foundation piles are loaded not only axially, but also laterally, introducing significant bending moments in the piles, which in turn cause bending stresses. Detailed studies of the lateral failure mechanism of historic quay walls were performed by Hemel et al. (2022, 2024). To accurately model and evaluate the timber piles supporting Amsterdam's historic quay walls, a proper estimate of their bending properties is essential. What sets these piles apart is their susceptibility to bacterial degradation (Harmsen and Nissen 1965; Varossieau 1949), which significantly impacts their strength and stiffness properties. Although historic foundations have been studied by numerous researchers, Aicher and Stapf (2016), Humar et al. (2021), and Pagella et al. (2022b) no research has yet

[1]Researcher, Faculty of Civil Engineering and Geoscience, Delft Univ. of Technology, Delft, CN 2628, Netherlands (corresponding author). ORCID: https://orcid.org/0000-0002-6704-5196. Email: m.hemel-1@tudelft.nl

[2]Senior Researcher, Faculty of Civil Engineering and Geoscience, Delft Univ. of Technology, Delft, CN 2628, Netherlands.

[3]Associate Professor, Faculty of Civil Engineering and Geoscience, Delft Univ. of Technology, Delft, CN 2628, Netherlands.

Note. This manuscript was submitted on November 2, 2023; approved on July 18, 2024; published online on October 28, 2024. Discussion period open until March 28, 2025; separate discussions must be submitted for individual papers. This paper is part of the ***Journal of Structural Engineering***, © ASCE, ISSN 0733-9445.

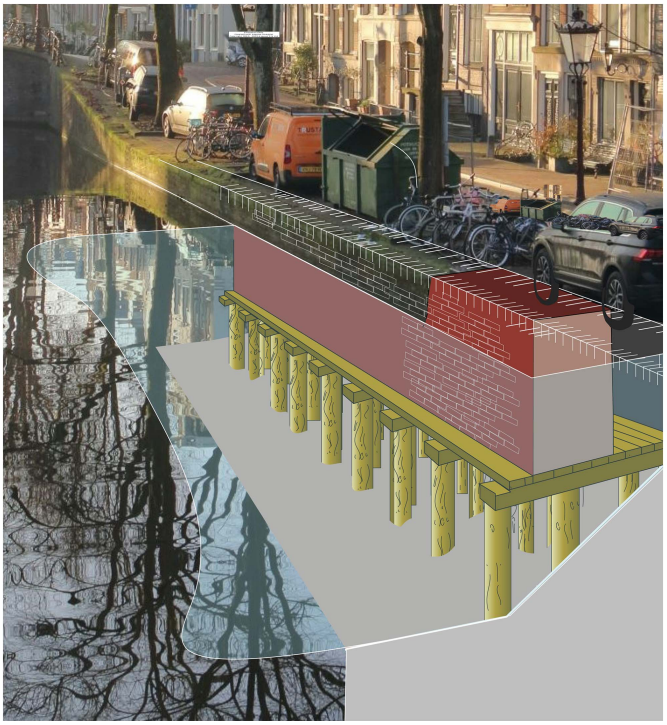

Fig. 1. Cutaway drawing of historical quay wall structure. Photograph taken at Reguliersgracht, Amsterdam, December 23, 2021. (Image by Mart-Jan Hemel.)

investigated the bending properties of historical timber foundation piles. This study filled this knowledge gap by conducting six four-point bending tests on spruce foundation piles from a historic 1905 quay wall in Overamstel, Amsterdam. Because variations in material properties were expected due to different diameters, the presence of knots, and bacterial decay, a four-point bending test was preferred because it can provide information on the flexural modulus of elasticity, the modulus of rupture, and the stress–strain behavior of the foundation piles over the full pile length. To account for the soft shell, nondestructive microdrillings are conducted. Before delving into the methodology, this study begins by presenting a review of the background literature, encompassing bending properties in practical applications, bending experiments on timber piles, and the impact of bacterial decay on timber piles.

Background Literature

Importance of Bending Properties and Use in Practice

In the modeling and assessment of timber piles, an important bending property is the bending modulus of elasticity, E_b. This modulus is defined as the ratio of stress to strain in the linear domain, and is a measure of a member's stiffness when subjected to bending moments. When modeling piles, the modulus of elasticity usually is combined with the moment of inertia I, resulting in the flexural stiffness EI to obtain the bending stresses σ_b. The ultimate bending strength of structural timbers is characterized by the modulus of rupture (MOR) (Cline and Heim 1912), which has been used for centuries to demonstrate the strength of wood (Thurston 1879). When stresses in timber exceed the MOR, the fibers are permanently damaged, resulting in plastic behavior. Currently, Amsterdam timber piles are assessed using the unity check $(\mathrm{UC}) = \sigma_{b,d}/\mathrm{MOR} < 1$, where subscript d refers to the design value. In the current assessment of quay walls, the Eurocode C24 (NEN 2016) timber class commonly is used. Typical C24 values are $E_{b,\mathrm{mean}} = 11{,}000$ MPa and $\mathrm{MOR} = 24\ \mathrm{N/mm^2}$ (characteristic fifth percentile).

Literature on Bending of Timber Piles

Bending tests are applied widely in a variety of research fields, such as wear of asphalt pavements (Pais and Harvey 2012), timber and steel beams (Chen and Lam 2013; Lim et al. 2013; Wang and Young 2016), ultimate flexural resistance in concrete (Yin et al. 2019) and medical (Kemper et al. 2007) and ecology applications, in which the strength of trees is tested (van Casteren et al. 2012). Bending tests give insight into the stress–strain response of a material and information on the modulus of elasticity, bending stresses, and bending strains ε. Two types of bending experiments commonly are used: three-point bending, and four-point bending. The fundamental difference is bending with shear (three-point bending) versus pure bending without shear (four-point bending). Another difference, which is of importance for this particular application, is the location of the maximal bending stress (Chitchumnong et al. 1989). In three-point bending, the maximum stress occurs directly at the load. In contrast, four-point bending tests produce a wider distribution of maximum bending stresses that extend between two applied loads. This distribution increases the likelihood that a larger portion of the tested material will be exposed to the maximum stress, which in turn raises the probability of encountering a weak spot within the sample. As a result, four-point bending tests may provide more comprehensive insights into the structural properties and failure mechanisms of the material being tested. For tapered piles, a constant bending stress between the loading points can be obtained by maintaining a certain force ratio. The force ratio is defined as $a_F = F_1/F_2$, where F_1 is the first point load, and F_2 is the second point load. Wilkinson (1968) stated that the force ratio should be proportional to the section modulus ratio between the two load points. This rule of thumb does not consider the self-weight of the pile.

For round timber members, many bending test studies have been performed in the past. A brief overview is given herein. Ranta-Maunus et al. (2011) used destructive and nondestructive methods to test more than 6,000 specimens of dry spruce and pine grown in several European countries. The average MOR was 40.2 $\mathrm{N/mm^2}$, and E_b was 11,200 MPa. Wilkinson (1968) conducted four-point bending and compression experiments on southern pine, red oak, and Douglas fir tapered members to determine the strength properties. For southern pine piles, E_b was 9,238 MPa and MOR was 12.5 $\mathrm{N/mm^2}$. The relation between timber densities and the modulus of rupture was studied by Cown and Hutchison (1983). Small-diameter ponderosa pine logs were tested in three-point bending by Larson et al. (2004), who found values of $E_b = 11{,}307$ MPa and $\mathrm{MOR} = 64\ \mathrm{N/mm^2}$ at the pile cap, and $E_b = 9{,}790$ MPa and $\mathrm{MOR} = 42\ \mathrm{N/mm^2}$ at the pile tip. Chilean radiata pine piles were subjected to bending tests and evaluated by Cerda and Wolfe (2003), who found an average E_b of 10,500 MPa. Lopez-Anido et al. (2003) investigated the effect of a composite fiber-reinforced polymer (FRP) shield to repair broken piles by performing three-point bending tests. Wolfe and Murphy (2005) compared the load capacity of small tapered round timber pile members with that of sawn timber members. The influence of the moisture content on the bending strength properties of round timber piles was researched by Ido et al. (2013), who found that the average strength of air-dried round timber was higher than that of green round timber.

The E_b value also can be determined by a number of nondestructive methods, such as transverse vibration (Green et al. 2006),

stress waves (Morales-Conde and Machado 2017), or nondestructive three-point bending (Christoforo et al. 2012) in which the midspan deflection w was limited to $w = L/200$ and $w = L/300$, where L is the length of the pile member.

Literature on Bacterial Decay on Timber Piles

Historical timber quay wall foundation piles can be as much as 300 years old. After hundreds of years in service, load carrying capacities of timber piles may be affected by load effects and biological deterioration (Buslov and Scola 1991; van de Kuilen et al. 2021). Two of the first fundamental studies of the degradation of timber piles were carried out by Varossieau (1949) and Harmsen and Nissen (1965). In recent years, more research has investigated the biological decay of historic pile foundations. Huisman et al. (2008) examined the relationship between timber degradation caused by erosion bacteria and the physicochemical properties of foundations with timber piles from sites in the Netherlands, Germany, and Italy. Klaassen and Creemers (2012) studied the behavior of timber foundations over time. Ceccato (2013) investigated the impact of wood degradation and soil creep on the behavior of timber pile foundations beneath historical buildings in Venice. An integrated finite-element analyses was conducted by coupling wood decay and soil creep.

Björdal and Elam (2021) examined nine timber foundation piles of spruce and pine in Gothenburg for fungal and bacterial degradation on a microscopic level. They stated that two parameters have a significant impact on the bacterial decay: time, and pile diameter. Other correlations between decay and spatial parameters could not be found. The most severe decay was present in the outermost layers of the piles, and had a thickness of 10–30 mm. This decay pattern often is referred to as soft shell. Thereafter the decay generally decreased and stopped at varying depths.

A study on 125-year-old timber piles below a building in Ljubljana was performed by Humar et al. (2021). Pandit and Patel (2022) characterized and assessed the compressive mechanical properties of spruce foundation piles obtained from bridges in Amsterdam. They conducted full-scale compression experiments on head, middle and tip parts of 12 foundation piles. The soft shell was investigated by microdrilling. It was concluded that microdrilling gives promising results for predicting the level of decay and making clear distinctions between healthy core wood and a decayed soft shell. Furthermore, it was concluded that compression failure occurred in more than 70% of the cases in sections with the highest density of knots (Pagella et al. 2022a).

Methodology

Bending Test Setup

To test the structural response of old timber foundation piles, four-point bending tests were performed. The test setup is shown in Fig. 2. The bending test setup is based on the principle of tensioning a bow. A pile with length L is held in place at the outer ends ($\overline{x} = 0$ and L) with support slings and tensioned by hoist slings attached to chain hoists in the middle ($\overline{x} = L_1$ and L_2). First, the pile is suspended by the two hoist slings without attaching the support slings at the ends. Due to its own weight, the pile deforms in an arch shape. Accordingly, the support slings at both ends of the pile are attached and the hoist chains are pulled until tension starts to develop at the support slings. This situation is considered the zero situation. At this moment, the pile is already subjected to bending stresses. The test starts and the pile is loaded by two point loads, which are applied by pulling the hoist chains step by step, increasing the bending stresses in the pile. A photograph of the bending test is shown in Fig. 3. The experiment is displacement controlled and a schedule of displacement targets is pursued.

The piles were extracted with a vibrating customized steel pneumatic clamp 3 m long to avoid pile breakage or damage. Of the six piles, the two piles that were in the best condition were equipped with fiber-optic (FO) wires, and the other four piles were left unchanged. The piles were stored fully submerged to ensure that the timber did not dry out and that the moisture content remained the same as it was prior to extraction. A schematic of the six piles that were used for the bending test is given in Fig. 4. A global reference system located at the original pile cap is indicated with (x, p) and for each pile, a local reference system $(\overline{x}, \overline{p})$ is provided. The length of the piles varied between 11 and 13 m. During extraction, Piles 1, 3, and 4 sustained damage. The pile diameter D, taper a, and wet density ρ_t of the tested population are presented in Table 1.

The wet density was assumed to be constant throughout the length of the pile, and was used solely for bending moment computations. The obtained results were comparable to values found in the literature for wet spruce foundation piles (Aicher and Stapf 2016; Pagella et al. 2022b). The wet density was determined by weighing the piles and dividing the result by their measured volume. Using a location-specific density along the pile length is unnecessarily complex, because for large imposed loads, the contribution of the self-weight of the pile to the moment distribution decreases, making a constant density more than sufficient. Furthermore, the diameter at $\overline{x} = 0$ is provided, indicated as D_L. Because the dimensions and length varied greatly among the piles, a unique loading configuration for each pile was used (Fig. 4). The support slings were connected to the pile at $\overline{x} = 0$ and L. The hoists were connected to the pile at $\overline{x}$= L_1 and L_2. The values of L, L_1, and L_2 are presented in Table 1, and are determined so that that the maximal stresses were present at about $x = L/3$ of the pile length. The ratio of the shear-free region to the total length for each pile is indicated as L_{sf}/L. For lateral loaded piles embedded in soil, this is the depth at which bending moments are expected to be maximal. Another important factor in the determination of L, L_1, and L_2 is the force ratio. This ratio should not be greater than 5 to assure the workability of the hoist cranes.

Load Ratio

The mechanical scheme for the four-point bending test on tapered piles is shown in Fig. 5. While performing the four-point bending test, it is important that stress in the most outer fiber σ_{outer} remains constant between the two loads F_1 and F_2. For tapered piles in which the self-weight is included, it is not possible to create a perfectly constant outer-fiber stress between the two loads because both the self-weight and the modulus vary over the pile length. It is however possible to find a solution for the F_1/F_2 ratio in which σ_{outer} at L_1 is equal to σ_{outer} at L_2, resulting in a more or less constant outer-fiber stress profile between L_1 and L_2 (Fig. 5). The ratio is determined analytically. An important assumption in the derivation of the force ratio is that the timber has a constant modulus of elasticity and is an isotropic and homogeneous material. Because E_b cannot be measured, this is the best assumption possible. The analytical derivation of bending moment formulas and the magnitudes of the force ratios is presented in Appendix I.

Instrumentation

The deflection of each pile was determined by an array of prisms for tachymetry with a spacing of 1 m across the entire pile length. Between each load step, the location of all prisms was measured

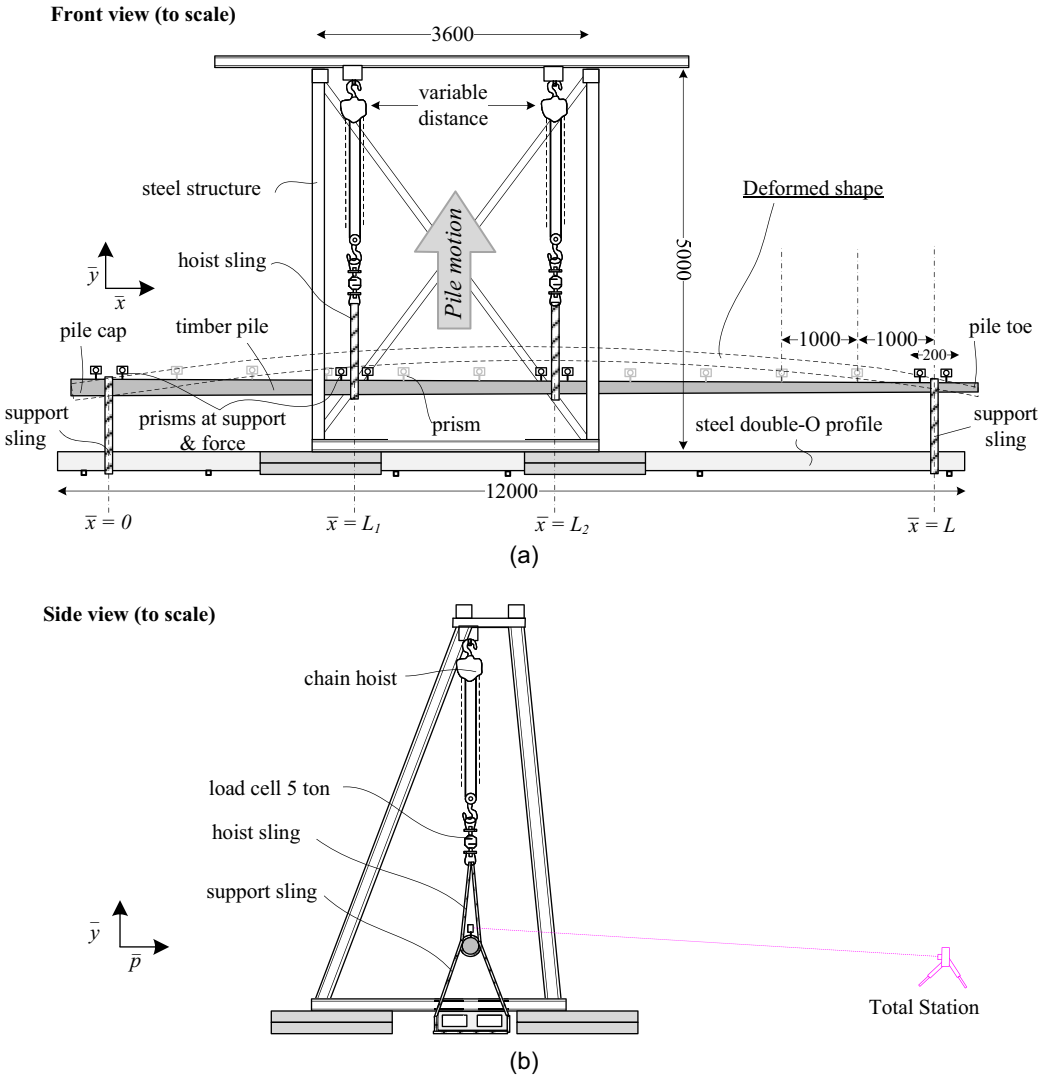

Fig. 2. Technical illustration of four-point bending experiment: (a) front view—the pile undergoes upward loading, leading to a deformed shape outlined by dashed lines; and (b) side view—total station employed to track pile deformation at various longitudinal locations.

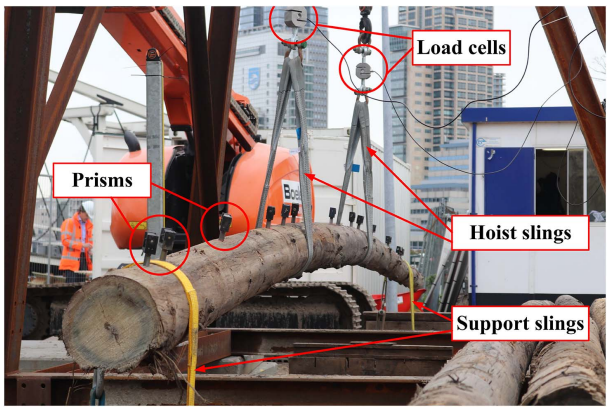

Fig. 3. Photograph of pile bending test setup during loading.

with a total station which had an uncertainty of 1 mm. From the displacement measurements across the pile length, the curvature κ of the pile in the bending plane was determined. To do so, a fourth-order polynomial function $y(x)$ was fitted using the displacement measurements to create a continuous deflection as a function of the pile length. Using the kinematic bending relation expressed in Eq. (1), the curvature as function of the pile length was determined. The loads in the hoist slings were measured by two 50-kN S-load cells. Force measurement was conducted at the sling connections, whereas displacement measurement occurred directly at the structure. Consequently, the extension of the slings had no discernible effect on the test outcome

$$\kappa = -\frac{d^2y}{dx^2} \tag{1}$$

Fiber-Optic Technique

In addition to the instrumentation described in the previous section, two piles—Piles 5 and 6—were equipped with fiber-optic wires to obtain the bending strains, curvatures, and deformations. For the OF-instrumented pile, two wires were glued inside the pile along the entire pile length. Each wire covered two perpendicular sides of the pile, starting from the pile cap toward the pile toe. The wire then went through the pile to the other side and was brought back to the cap. In this manner, the wires were installed in a quadrant orientation (Fig. 6). The two wires were labelled north–south (N-S)

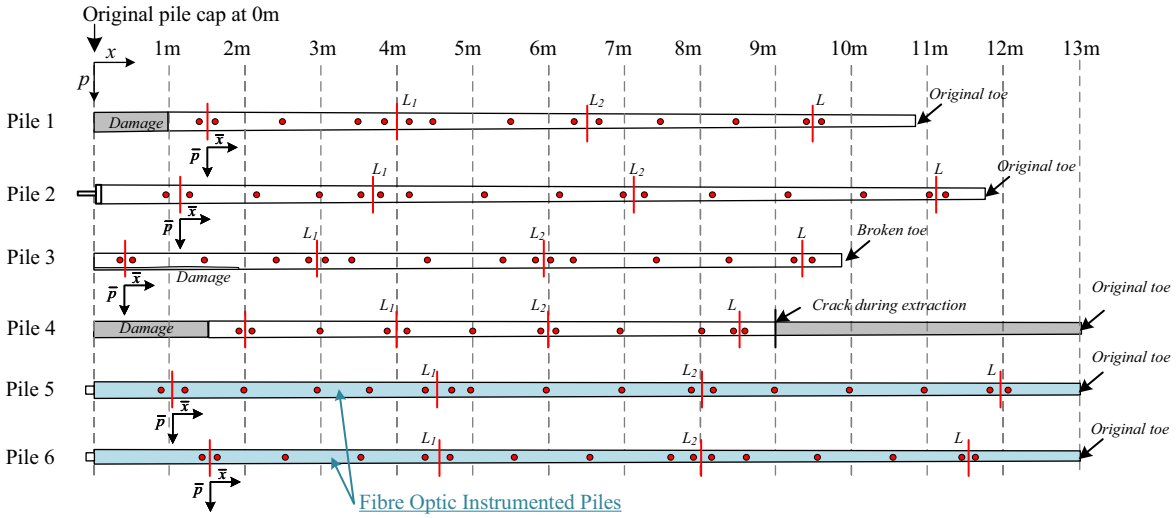

Fig. 4. Top view of piles for the four-point bending test. Shaded areas at the pile cap and pile tip indicate the removed sections. The solid circle marks the measuring prism, and the vertical bolt line shows the support or hoist point. The bottom two piles have FO installed.

Table 1. Pile properties and their loading dimensions with respect to their local reference $(\bar{x}, \bar{p})$

Pile no.	a (m/m)	ρ_t (kN/m^3)	$(\bar{x}, \bar{p})$ (m)	D_l (m)	L_1 (m)	L_2 (m)	L (m)	L_{sf}/L
1	0.01109	7.10	1.5	0.259	2.5	5.0	8.0	0.22
2	0.00703	6.58	1.1	0.233	2.5	6.0	10.0	0.20
3	0.00620	7.59	0.4	0.240	2.5	5.5	8.9	0.12
4	0.00578	7.15	2.0	0.214	2.0	4.0	6.5	0.15
5	0.00679	7.20	1.0	0.228	3.5	7.0	11.0	0.18
6	0.00884	7.18	1.5	0.245	3.0	6.5	10.0	0.30

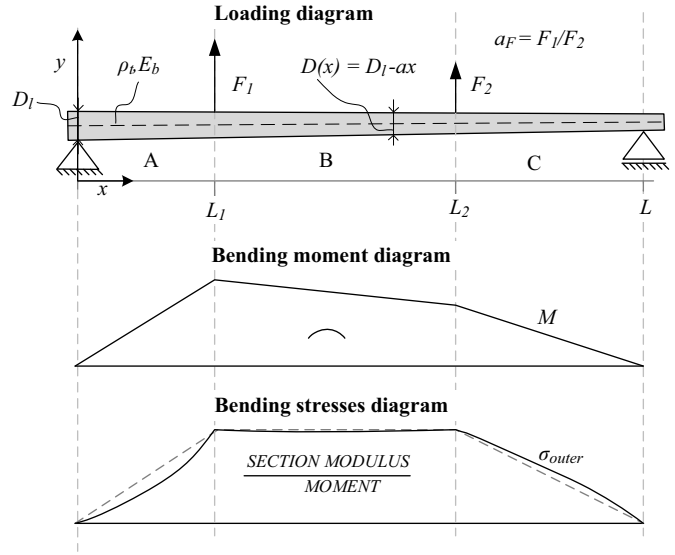

Fig. 5. Mechanical scheme four-point bending test on tapered pile. Dashed trapezoid in bending stress diagram is provided to show nonlinearity in bending stresses.

and east–west (E-W). The center-to-center distance between north and south is denoted h_{NS}; perpendicular to that, the east–west distance was denoted h_{EW}. A quadratic orientation was essential, because with two fibers the curvature can be determined in only one plane. Any deviations φ_r between the fiber orientation plane and the plane of actual bending would result in an underestimation of curvature, and thus of displacement (Fig. 7). By installing the fibers in four main directions the curvatures κ_{NW} and κ_{EW}, in the N-W and E-W directions, can be computed from the strain measurements along the pile length according to Eq. (2), where ε_N, ε_S, ε_E and ε_W are the measured strains in the north, south, east and west fibers, respectively. Because the curvature is a vector, the total curvature in the plane of bending κ_t can be computed using Eq. (3). The fibers had a spatial resolution of 0.25 m, indicating the system's capability in fiber-optic measurements to discern fine spatial details along the fiber's length, thereby determining the smallest detectable features

$$\kappa_{NS} = \frac{\varepsilon_N - \varepsilon_S}{h_{NS}} \qquad \kappa_{EW} = \frac{\varepsilon_E - \varepsilon_W}{h_{EW}} \tag{2}$$

$$\kappa_t = \sqrt{K_{NS}^2 + K_{EW}^2} \tag{3}$$

From the resultant curvature κ_t across the pile length, the deflections y can be obtained according to Eq. (4). The derivation of Eq. (4) is presented in Appendix II

$$y(x) = -\frac{(\int_0^L (1-x)\kappa_t(x)dx)x - L(x(\int_0^x \kappa_t(x)dx) - (\int_0^x x\kappa_t(x)dx))}{L} \tag{4}$$

Microdrilling Measurements to Determine Soft Shell

For this bending experiment, it was essential to determine the thickness of the soft shell to estimate the effective diameter h. It is

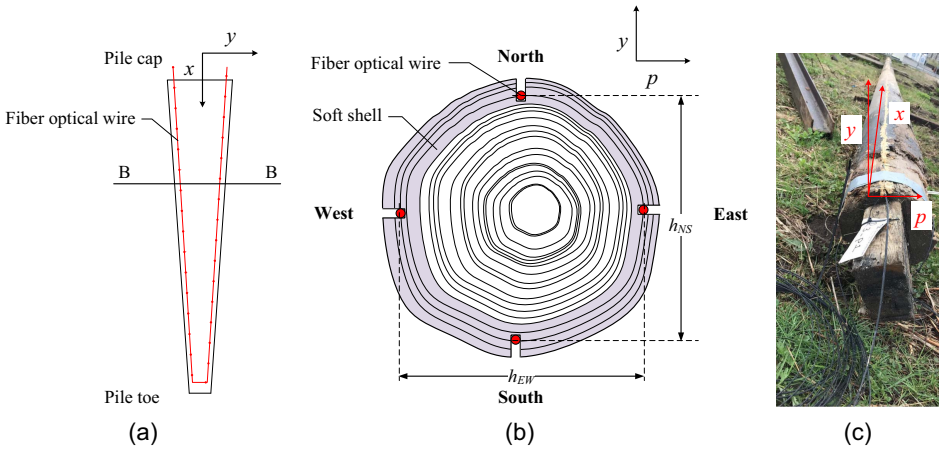

Fig. 6. Fiber-optic wire orientation: (a) side view of pile with W-E fiber-optic wire; (b) sectional view of the quadratic orientation of the fibers; and (c) fiber-optic wires installed in the timber pile.

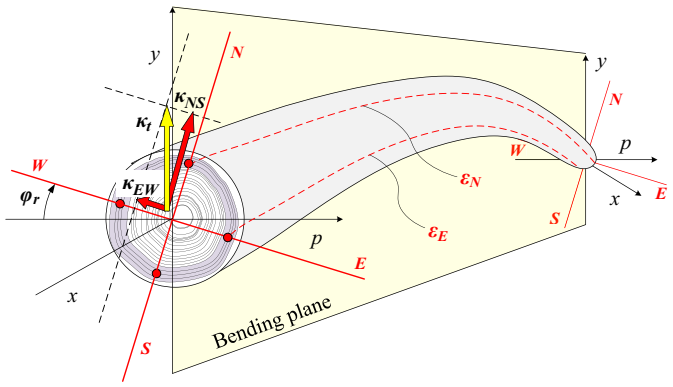

Fig. 7. Schematic depiction of a bending-loaded pile. Pile reference system denoted (x, y, p), where x is along the pile axis and y is the bending direction. Fiber-optic reference system denoted (N-S,E-W), rotated by angle φ_r relative to bending plane.

Fig. 8. IML microdrilling performed on piles after the bending tests took place.

important to exclude the soft shell from the strength analysis of the timber pile because the soft shell has very little structural strength. Using an external diameter underestimates the modulus of elasticity E_b and the MOR of the heartwood. Bending capacity tests of timber piles also need to be conducted using the effective diameter instead of the external diameter. To estimate the soft shell, the microdrilling method using an IML-RESI PD [Instrumenta Mechanik Labor System GmbH (IML), Wiesloch, Germany] was used (Fig. 8). This method is used widely for timber in general, and currently an IML-RESI is in the trial stage for underwater use in the historic center of Amsterdam. An extensive analysis of the microdrilling resistance and the positive and negative aspects of the IML technology was carried out by Gard and van de Kuilen (2018). The IML-RESI PD had a drilling tip of 3 mm at the tip, which converged to a shaft of 1.5 mm. The drill was pushed while drilling with a constant feed through the timber. Two parameters are important when drilling: the feed resistance Ω_f, and the drill resistance Ω. Both resistances were measured, and an example as a function of the drilling depth is presented in Fig. 9. The outer vertical lines denote the pile's diameter, the inner vertical lines represent effective diameter h, and distance between them indicates the soft shell. Large densities, for example knots, are evident as large amplitude peaks. Furthermore, year rings can be identified by high frequency wiggles. Low resistance

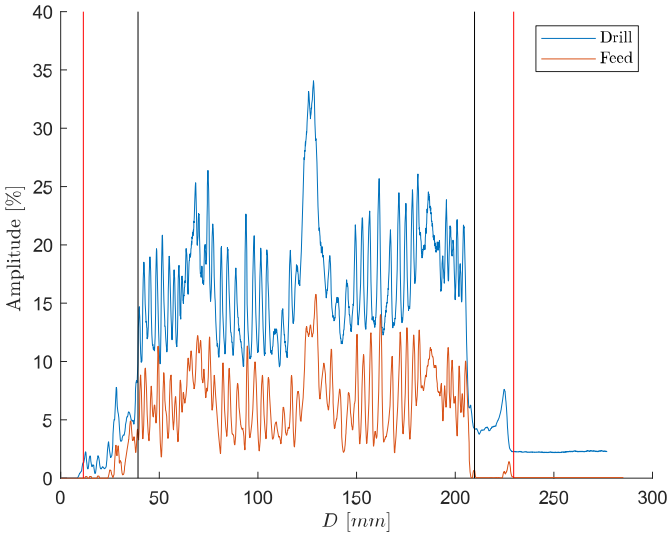

Fig. 9. Microdrill test data showing drilling resistance profile of pile.

amplitudes can indicate cavities, low-quality timber, or degraded timber. At various locations along the piles, microdrillings were performed in the plane of bending after the bending tests took place.

Results and Interpretations

Moment–Curvature Diagrams

To obtain the moment–curvature (M-κ) diagrams, the curvature and bending moment diagrams first need to be constructed. For illustration purposes, the deflection, curvature, and moment of Pile 5 are provided in Fig. 10. Not all load steps are visualized in order to keep the figure clear. Using the deflection prism measurements, fourth-order polynomial functions $P_w(x)$ were fitted. From the deflections, the curvature along the pile length was determined as $\kappa = -d^2P_w(x)/(\mathrm{d}x^2)$ according to Eq. (1). Because the curvature was obtained from the second derivative of a polynomial fit through discretized prisms, small errors were expected. Especially at the supports, errors can occur where in theory curvatures should be zero. An interval along the x-axis was chosen within which the curvature was considered to be useful for analysis, indicated in Fig. 10 with dashed vertical lines at $x = 2$ and 9 m. Expressions for the bending moment along the x-axis are provided in Appendix I.

Fig. 11 presents M-κ for various cross sections along the x-axis for Pile 5. The M-κ diagrams follow a linear trajectory that transitions into an elastic-plastic behavior. The gradient of the linear trajectory is associated with the flexural stiffness EI of the pile, and was largest at the cap of the pile ($x = 2$ m) and smallest at tip of the pile ($x = 9$ m). This was expected because the piles are tapered, and have a larger diameter at the cap than at the tip. The pile broke at $x = 6.5$ m, which is indicated with a star in Fig. 11. Bending moments already occurred when the curvature in the pile was zero. This was because the prisms were measured initially when the pile bent due to its self-weight in the hoist slings. Therefore it was essential to shift the M-κ curves along the κ-axis so that the slope of the linear part passed exactly through the origin.

Fiber-Optic Results

For Pile 5, the measured strains in the north–south direction are presented in Fig. 12. The N-S direction was considered to be in the direction of bending. The horizontal axis of Fig. 12 indicates the wire length, and the vertical axis indicates the macrostrain $\mu\varepsilon$. Between 101.176 and 113.173 m, the wire was in the open air, and entered the pile cap at $\overline{x} = 0$ m. The wiggles in Fig. 12 were caused by temperature influences. From 113.173 to 124.403 m, the north strain was measured between the two support slings. Between 124.403 and 126.445 m, the wire ran to the pile tip and back to the support at $\overline{x} = L$. From 126.445 to 137.675 m, the south strain was measured between the two support slings. From 127.675 to 157.584 m, the wire left the pile and was in the open air. The fiber broke directly after Loading step $F_1 = 9.16$, $F_2 = 2.28$ kN, with a

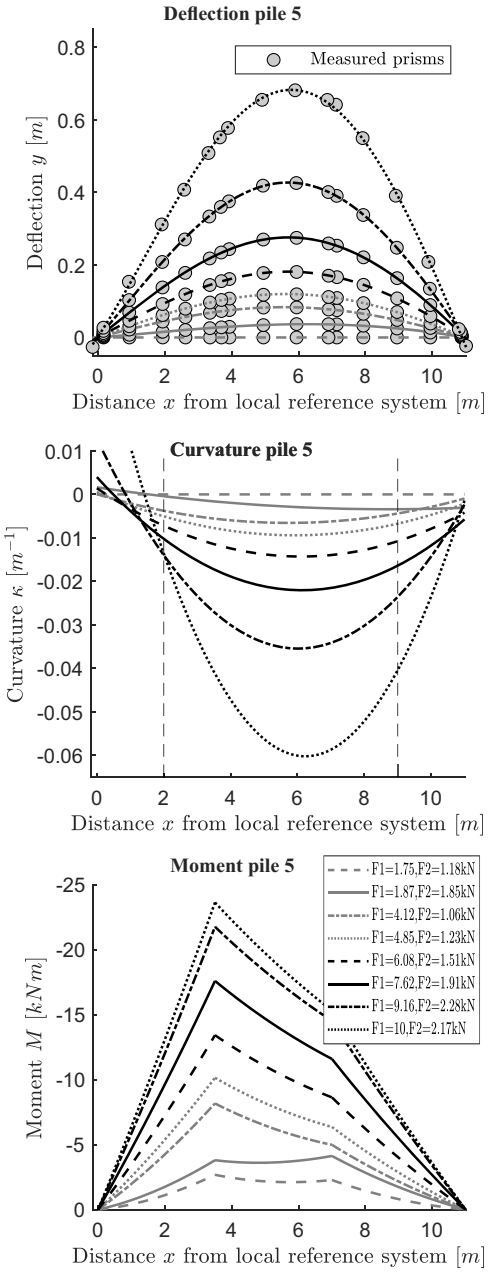

Fig. 10. Deflection, curvature, and moment diagrams of Pile 5. Not all load steps are visualized.

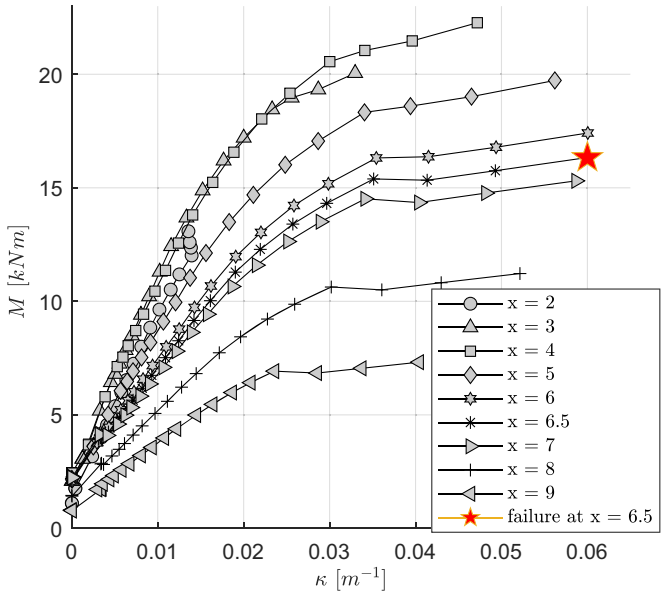

Fig. 11. M-κ diagram of Pile 5 for different cross sections along the x-axis.

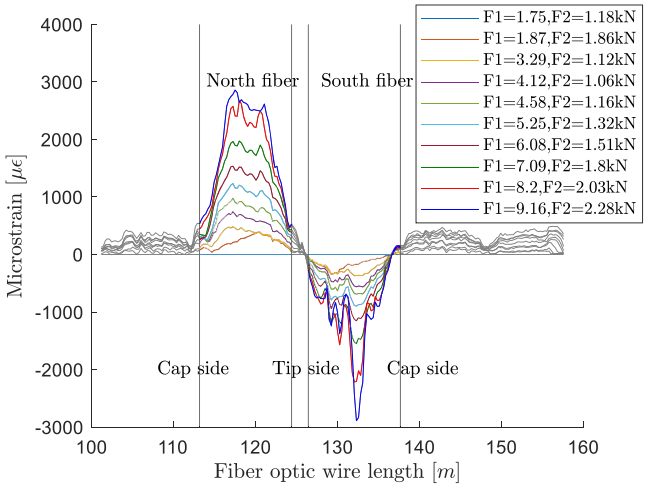

Fig. 12. Measured strain in north–south direction of Pile 5.

maximal strain of 2,800 $\mu\varepsilon$, which was earlier than the breakage of the pile itself.

The strain in the north fiber and the south fiber were not symmetrical, especially for the larger loads. The strain at the north fiber had a trapezoidal profile, as intended (Fig. 5). However, for the south fiber, this was not the case. Large peaks appeared in the measured strain at Loading step $F_1 = 7.09$, $F_2 = 1.8$ kN, and the strain profile narrowed. Peaks started to form at 1,550 $\mu\varepsilon$ in the south fiber, and no significant peaks were observed in the north fiber. Nevertheless, the maximal strain in the north fiber was more or less equal to the maximal strain in the south fiber. The difference between the compression and tension profiles was due to the anisotropic nature of the timber, which sometimes included twisted fiber directions. Consequently, the stress profiles were asymmetric, and the tension side often exhibited stronger nonlinearity. Additionally, peaks in the compression side may be attributed to measurement errors caused by high local stresses compressing the fiber-optic wire at certain points. In the east–west direction, the measured strains remained below 500 $\mu\varepsilon$, which is a sign that the orientation of the north–south direction was in good alignment with the plane of bending. The FO-computed curvature and prism-obtained curvature $P_w(x)$ of Pile 5 is presented in Fig. 13. The FO curvatures

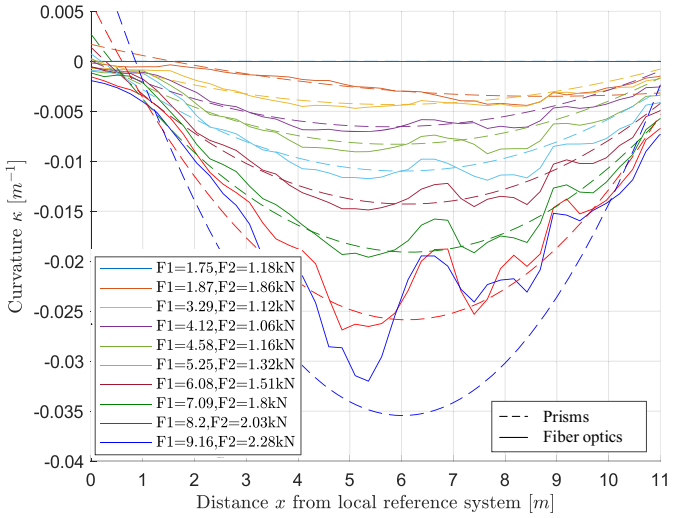

Fig. 13. Curvature of Pile 5 obtained from fiber strains.

matched the prism curvatures well until Load step $F_1 = 9.16$, $F_2 = 2.28$ kN. After that, computed curvatures from FO measurements became poor because the fiber started to crack. At $x = 6.5$ m, a small bump occurred, which increased in size with increasing load. This is the location at which the pile ultimately broke.

For Pile 6, the fiber broke with a maximal strain of 2,500 $\mu\varepsilon$, which was slightly less than the strain at which the fiber in Pile 5 broke, 2,800 $\mu\varepsilon$. Large peaks and deep troughs started to appear in the signal, mainly in the south fiber, when loads increased and strains approached 1,600 $\mu\varepsilon$. Above 1,600 $\mu\varepsilon$, curvature predictions became poor due to the disturbed strain signal, which is comparable to the situation for Pile 5, in which predictions became poor at 1,550 $\mu\varepsilon$.

Flexural Stiffness along Pile

For each location along the pile x-axis, the moment–curvature diagram was constructed and EI was determined. This process was repeated for all six piles, resulting in the flexural stiffness along the x-axis of each pile (Fig. 14). For all piles, the flexural stiffness was greatest at the pile cap and smallest at the pile toe. The flexural stiffness determined using fiber optics was in good alignment with the flexural stiffness obtained using the prism measurements.

In the determination of the flexural stiffness, only a certain range of the pile length was considered. Firstly, the support slings were not connected to the outermost ends of the pile, resulting in the absence of bending information at those extreme parts. The second reason had to do with the uncertainty in the curvature and bending moment measurements close to the sling supports. Because both the curvature and the moment approach zero at the location of the supports, errors become infinitely large at $\bar{x} = 0$ and $\bar{x} = L$. Close to the supports, the determination of the flexural stiffness is considered to be unreliable, and therefore was excluded.

Effective Diameter with MicroDrilling

As described in the "Methodology" section, microdrill measurements were performed in order to estimate the soft shell. During the bending experiments, the appearance of the soft shell became visible. Fig. 15 shows the soft shell cracked open from the healthy

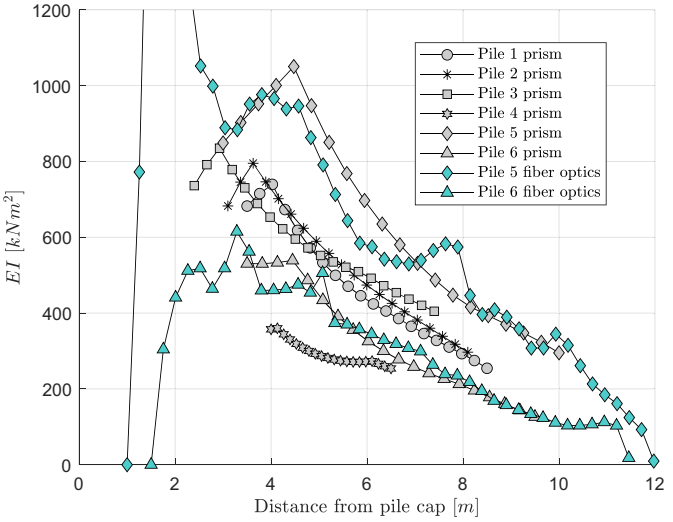

Fig. 14. Flexural stiffness of Piles 1–6 across pile length obtained using prism method and for Piles 5 and 6 using fiber optics method.

Fig. 15. Soft shell visible during loading of Pile 4 at Load step 14 of 26. The soft shell cracked open.

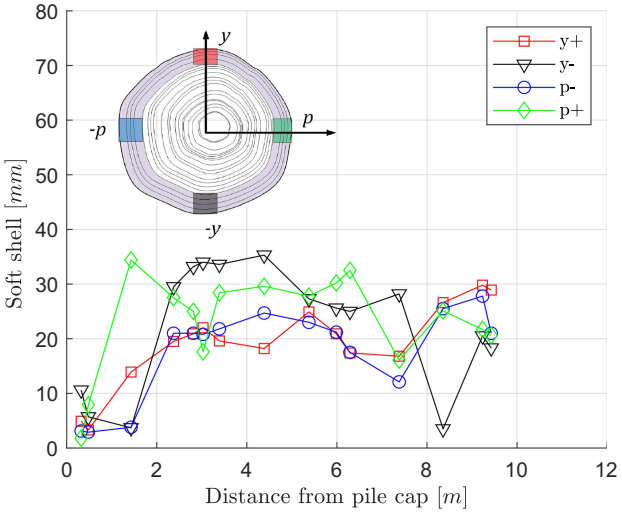

Fig. 16. Soft shell estimate of Pile 3.

heartwood. During this process, the forces in load cells hardly changed, indicating that the soft shell had a neglectable influence on the bending of the pile. For all piles, the soft shell moved like a sleeve around the heartwood, and had no significant contribution to the bending resistance. The estimated soft shell for Pile 3, based on IML measurements, is presented in Fig. 16. The thickness of the soft shell was less than 10 mm at the pile cap, but 2 m from the cap the softshell thickness increased to 20–35 mm. The spatial variability of the thickness of the soft shell was significant, and was present for all piles. No correlation between pile diameter and soft shell thickness was found, nor was any correlation between soft shell and longitudinal pile location, indicating that the biological decay of timber piles had a large arbitrary spatial variety. The mean soft shell thickness of the population was 21 mm, with a 95% characteristic value of 36 mm. Fig. 17 shows a cross-sectional photograph of Pile 3 directly after the breakage at 5 m from the pile cap. The soft shell is indicated with a dashed white line; the texture of the timber shell was different from that of the heartwood. The thickness of the soft shell was 25 mm in the north–south direction, which was in good correspondence with the IML drillings.

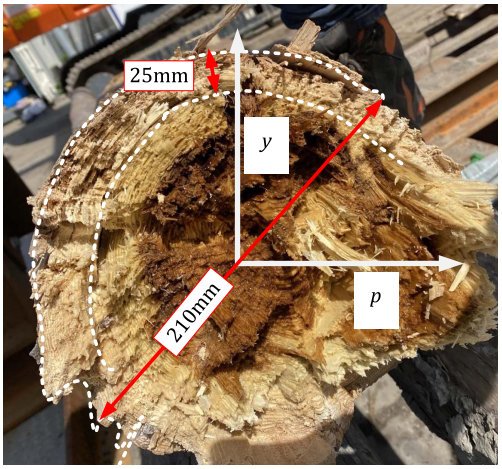

Fig. 17. Photograph of bending failure cross section of Pile 3. The soft shell can be identified by the color and structure of the timber fibers.

Modulus of Elasticity

The modulus of elasticity (E_b) was computed using Eq. (5), in which the determined flexural stiffness $\widetilde{EI}$ is divided by the moment of inertia based on an effective pile diameter h

$$E_b = \frac{\widetilde{EI}\,64}{\pi h^4} \tag{5}$$

The effective diameter h was determined at each prism location, so the modulus of elasticity was determined only at these points. The elastic modulus as function of the pile length is presented in Fig. 18. Measurements close to the sling supports are excluded due to measuring uncertainties. The modulus of elasticity varied greatly. Even given the large spread, there was a trend between the pile location and modulus of elasticity: E_b was roughly 2 times higher at the cap than at the toe. This can be attributed to the growth pattern of the tree, because the pile cap, which was at the bottom of the tree, experienced greater preloading than the top when the tree was alive. The correlation coefficient for all measurements was $\rho = -0.41$, the correlation of individual piles is, in order of the pile number, $\rho = -0.64$, -0.75, -0.62, -0.81, -0.14, and 0.40. The correlation within a specific pile was higher than that for the

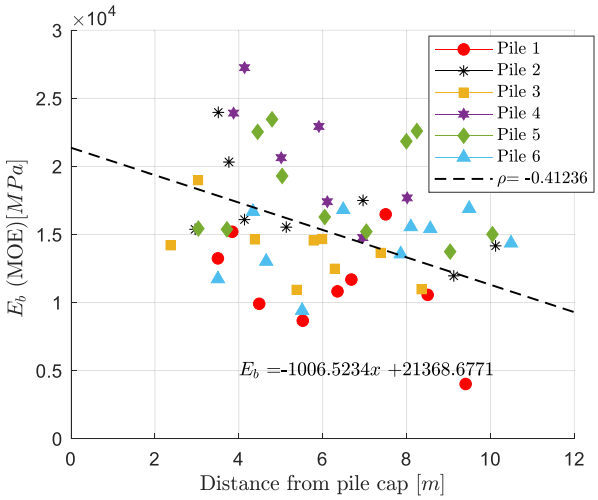

Fig. 18. Modulus of elasticity as function of the pile length.

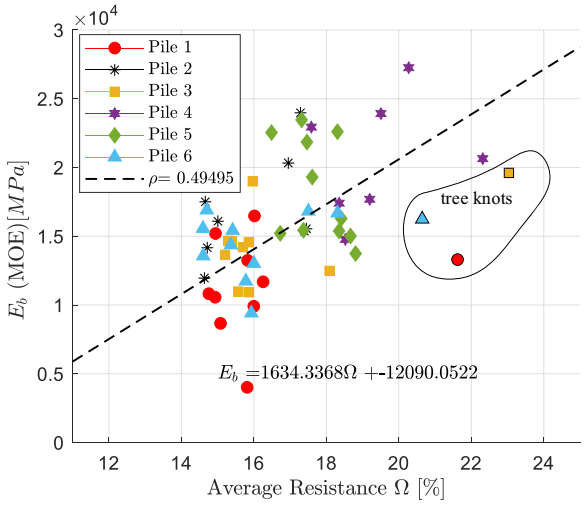

Fig. 19. Modulus of elasticity as function of the average IML drilling resistance. Because of their high Ω, tree knots are excluded from linear regression.

entire population, except for Pile 5, which again underlines the large spread between and within the different piles. The average E_b value was 16.5 GPa.

To estimate the modulus of elasticity based on IML drillings, the modulus of elasticity is plotted as function of the average drill resistance Ω in Fig. 19. The drilling resistance and modulus of elasticity were moderately correlated ($\rho = 0.50$). The larger the drill resistance, the larger was the modulus of elasticity. The determination of E_b had uncertainties due to a varying soft shell thickness and material variability. The average drilling resistance also was influenced by the same factors. Plotting E_b against resistance created an amplifying effect, resulting in wide data dispersion per pile (Fig. 19). The correlation between E_b and resistance broke down within individual piles but was significant between piles. Therefore, focusing on a trend per pile is unnecessary; instead, attention should be given to the trend based on data from all piles.

Modulus of Rupture

To determine the modulus of rupture, the moment–curvature outcomes from the experiment were compared with the theoretical moment–curvature relation for a circular cross section containing elastic–perfectly plastic material properties. To do so, the moment M and curvature κ were normalized according to their first yield values M_0 and κ_0, resulting in $M^* = M/M_0$ and $\kappa^* = \kappa/\kappa_0$. The yielding values were derived from the M-κ diagram at the point at which deviation from the linear trajectory occurred. The normalized theoretical moment–curvature diagram, including normalized experimental data, is presented in Fig. 20(a). Only experimental data for which yielding was present were used. Mathematical expressions for the theoretical normalized moment–curvature of a circular cross section are given in Eqs. (6) and (7), where $\sin(a^*) = 1/\kappa^*$ (Pandit and Patel 2022). The stress–strain diagram of an elastic–perfectly plastic material is shown in Fig. 20(b). For $0 < \kappa < \kappa_0$, the diagram is linear and associated with the linear-elastic phase. All cross-sectional stresses remain below the MOR. For $\kappa > \kappa_0$, the outer fiber stress becomes larger than the MOR, which is associated with the elastic–plastic phase. The limit value which the bending moment reaches is found when the curvature becomes infinitely large. At this point, all fibers are fully plastic, with a stress equal to the MOR. The piles followed the theoretical elastic–perfectly plastic trajectory in good correspondence except for Pile 4, which showed hardening behavior for curvatures larger than $\kappa^* = 2$

$$\kappa^* \le 1 \qquad M^* = \kappa^* \tag{6}$$

$$\kappa^* > 1 \qquad M^* = \frac{16}{3\pi}\left(1 - \frac{1}{\kappa^{*2}}\right)^{3/2} + \frac{2\kappa^*}{\pi}\left(a^* - \frac{\sin(4a^*)}{2}\right) \tag{7}$$

Because of the strong correlations found, the timber is described as an elastic–perfectly plastic material. Therefore, it was possible to determine the stress–strain relationship and thus the MOR. Relationships between bending stress and bending strain are provided for the elastic phase in Eq. (8) and for the elastic–plastic phase in Eq. (9). Because E_b, strain ($\varepsilon = \kappa h/2$), bending moment M, and h are known, one can determine σ and construct the stress–strain diagram. The derivation of Eq. (9) is presented in Appendix III

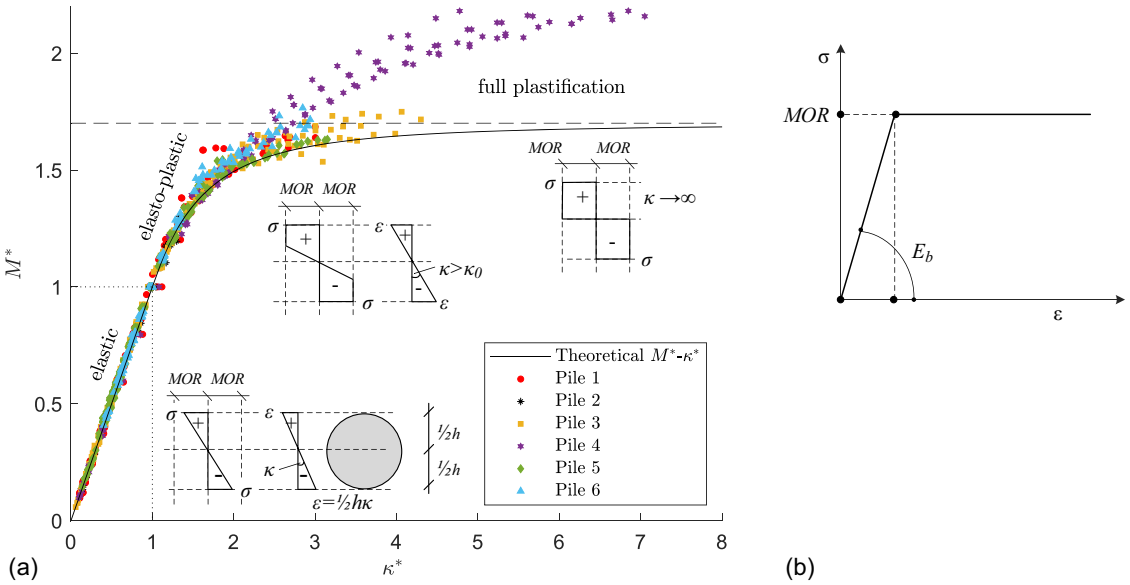

Fig. 20. (a) Normalized moment–curvature diagram based on a circular cross section with bilinear stress–strain behavior, with measurements normalized according to $M^* = M/M_0$ and $\kappa^* = \kappa/\kappa_0$; and (b) bilinear stress–strain diagram.

$$\kappa^* \le 1 \qquad \sigma = \varepsilon E_b \tag{8}$$

$$\kappa^* > 1 \qquad M = \frac{h^3\left(\left(\frac{8}{3}E_b^2\varepsilon^2\sigma - \frac{8}{3}\sigma^3\right)\sqrt{\frac{E_b^2\varepsilon^2-\sigma^2}{E_b^2\varepsilon^2}} + E_b^3\varepsilon^3\left(\arcsin\left(\frac{\sigma}{E_b\varepsilon}\right) - \frac{\sin\left(4\arcsin\left(\frac{\sigma}{E_b\varepsilon}\right)\right)}{4}\right)\right)}{16E_b^2\varepsilon^2} \tag{9}$$

The stress–strain diagrams for all six tested piles in bending are provided in Fig. 21. Multiple lines are plotted for each pile, representing yielding positions along the length of the pile at the same spots at which IML drillings were conducted. The slope of the linear trajectory is defined by E_b and the plastic limit by MOR. Pile 4 showed hardening behavior, whereas the other piles had a more or less constant plastic limit with an increasing strain. Fig. 21 also presents a histogram of the MOR with a 90% confidence interval. The mean modulus of rupture was 23.16 N/mm^2, with a standard deviation of 6.9 N/mm^2. The modulus of rupture varied widely, from 13 to 40 N/mm^2. The spread within each pile was smaller but still significant. It can be concluded that the common practice of using a C24 timber strength class for evaluating quay wall piles can be differentiated. For example, some of the piles may have lower strength, making a C18 class more accurate. In addition, there are cases in which a C24 class is too conservative, and higher strength classes should be considered.

Fig. 22 plots the MOR as function of the location along the pile axis. The MOR had a very poor correlation with the location along the pile axis. The relation between the IML drill resistance and the MOR is provided in Fig. 23. A moderate correlation, $\rho = 0.65$, was found, which indicates that a higher drill resistance corresponded to a higher modulus of rupture.

To illustrate the effect of using an effective diameter h, Fig. 24 plots E_b versus MOR. Strength parameters determined using external diameter D are indicated with solid circles, whereas strength parameters computed using effective diameter h are indicated with solid squares. Including or excluding the soft shell had a large impact on E_b and MOR. Both quantities were strongly correlated ($\rho = 0.83$). Fig. 24 also includes data from a study of historic foundation bride piles by Pagella et al. (2022b). They tested fully saturated spruce timber foundation piles in compression. The piles were extracted from foundations of two demolished historical bridges in Amsterdam. Pagella et al. (2022b) found a very similar MOR– E relation to that from the present study.

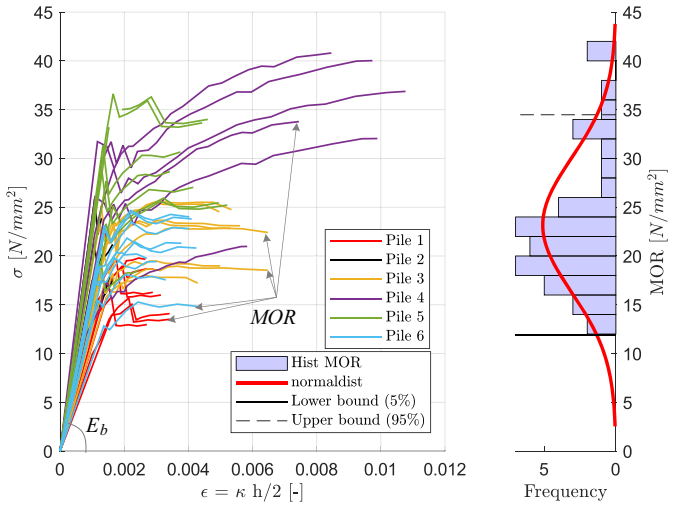

Fig. 21. Stress–strain behavior of timber piles in bending. Horizontal part of bilinear curve is defined as modulus of rupture MOR, and linear trajectory is defined as modulus of elasticity E_b.

Conclusion

From this study, the following conclusions were drawn:

- The mean value of E_b was found to be 16.5 GPa, with variation coefficient 0.30, whereas the MOR had a mean value of

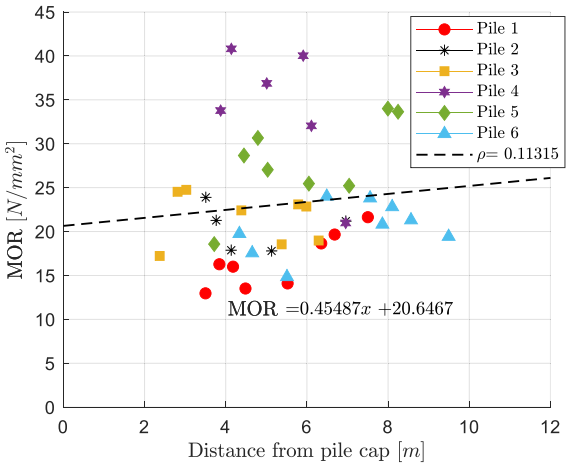

Fig. 22. MOR as function of the pile length.

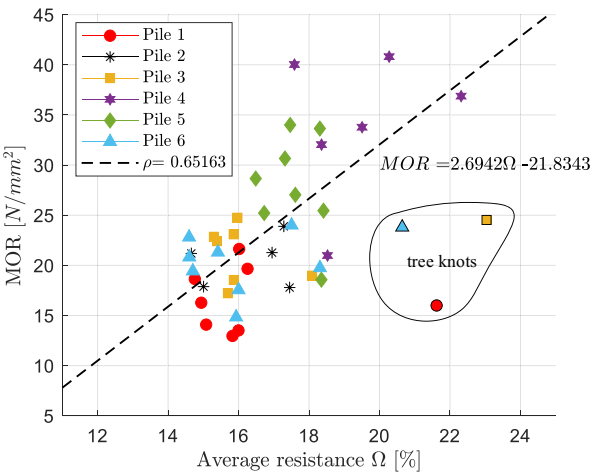

Fig. 23. MOR as function of the average IML drilling resistance. Tree knots are excluded from linear regression.

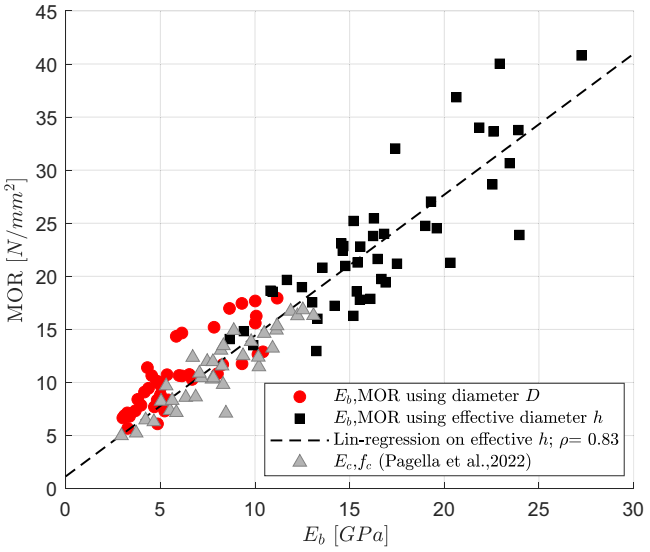

Fig. 24. MOR versus E_b. Solid circles indicate strength parameters determined using outer diameter D. Solid squares indicate strength parameters computed using effective diameter h. A regression line is presented through the effective diameter data. Compressions strengths of Pagella et al. (2022b) are provided.

23.2 N/mm^2, with variation coefficient of 0.26. There was a significant variation in both E_b and MOR values among the piles. Analyzing a single pile at multiple locations along its length found a smaller spread in values, but it still was significant. Despite the spread between individual piles, a strong correlation, 0.83, was found between the modulus of elasticity and the modulus of rupture.

- In situ surveying of timber strength is necessary to obtain a better estimate of the strength of urban foundation piles. The strength of foundation piles in Amsterdam varies significantly, making it inadequate to rely solely on a single strength class, as currently is done using the C24 class for historic quay walls.
- For five piles, a bilinear elastic–perfectly plastic material behavior was observed in which the plastic limit was reached at 1,800 $\mu\varepsilon$. One of the piles showed considerable hardening behavior.
- Microdrilling is a promising technique for estimating bending strength parameters and determining the soft shell. The correlations between IML microdrill resistance and the modulus of elasticity and modulus of rupture were found to be 0.65 and 0.5, respectively.
- Bacterial deterioration appears to be independent of both the outer pile diameters and the location along the timber pile. An in situ IML drilling at the pile cap on a pile foundation does not provide a comprehensive assessment of the deeper parts of the same pile. On average, a soft shell 21 mm thick was found, and the maximum value was 45 mm.
- The insertion of fiber-optic wires into historic foundation piles to measure bending strains is an effective instrumentation tool, because they can measure values as great as of 1,600–2,000 $\mu\varepsilon$. However, when larger strains are present, the accuracy of the measurements becomes compromised, because strain peaks appear in the measured signal, eventually followed by breaking of the FO wires. The failure of FO wires can be attributed to their connection with the timber fibers, which undergo permanent deformation at approximately 1,800 $\mu\varepsilon$. This deformation causes stress concentration in the FO wires, ultimately leading to their failure.

When performing bending capacity checks of timber piles, it is recommended to use effective diameter instead of external diameter. For geotechnical computations, it is advised to use external diameter, including the soft shell. Time effects such as timber creep were not studied, but can be of significant importance when assessing timber foundations in bending over a long time span.

Appendix I. Bending Moment and Force Ratio

The pile deflection y is described using an Euler–Bernoulli beam, the bending equation of which is provided in Eq. (10), where ρ_t is the determined wet density of the timber (kg/m^3), a is the measured taper of the pile (m/m); and D_l is the measured diameter at the location of the local reference system (m)

$$\frac{d^2}{dx^2}\left(E_b\frac{\pi(D_l-ax)^4}{64}\frac{d^2y}{dx^2}\right)=\rho_t\frac{1}{4}\pi(D_l-ax)^2 \tag{10}$$

The pile is divided into three fields, A, B, and C, for which the general solution of each field is presented in Eq. (11), where A_i, B_i, and C_i are integration constants

$$y_j(x)=\frac{\left(\frac{j_1}{D_l-ax}+\frac{j_2}{(D_l-ax)^2}+\frac{4\rho_t x^2}{E_b}\right)}{6a^2}+j_4x+j_3 \quad j=A,B,C \tag{11}$$

To solve the system of equations, the boundary and interface conditions in Eq. (12) are used, where rotation φ (rad), bending moment M (kNm), and shear force V (kN) are described by the kinematic and constitutive relations in Eq. (13)

$$\begin{aligned}
&x=0\rightarrow && y_A=0 && M_A=0 && && \\
&x=L_1\rightarrow && y_A=y_B && M_A=M_B && V_A=V_B+F_1 && \varphi_A=\varphi_B\\
&x=L_2\rightarrow && y_B=y_C && M_B=M_C && V_B=V_C+F_2 && \varphi_B=\varphi_C\\
&x=L\rightarrow && y_C=0 && M_C=0 && &&
\end{aligned} \tag{12}$$

$$\varphi(x)=-\frac{dy}{dx};\qquad M(x)=-E_b\frac{\pi(D_l-ax)^4}{64}\frac{d^2y}{dx^2};\qquad V(x)=-E_b\frac{\pi(D_l-ax)^4}{64}\frac{d^3y}{dx^3} \tag{13}$$

Substituting the general solutions of Eq. (11) into the boundary and interface conditions [Eq. (13)] results in a system of equations. Solving this set of equations results in the following bending moment equations for fields A, B, and C

$$M_A(x) = \frac{(L^4\pi a^2\rho_t - 4D_lL^3\pi a\rho_t + 6D_l^2L^2\pi\rho_t + (-x\pi(a^2x^2 - 4D_lax + 6D_l^2)\rho_t - 48F_1 - 48F_2)L + 48L_1F_1 + 48F_2L_2)x}{48L}$$

$$M_B(x) = \frac{L^4\pi a^2\rho_t x - 4D_lL^3\pi a\rho_t x + 6D_l^2L^2\pi\rho_t x + (-\pi a^2\rho_t x^4 + 4\pi D_l a\rho_t x^3 - 6D_l^2\pi\rho_t x^2 - 48L_1F_1 - 48F_2 x)L + 48x(L_1F_1 + F_2L_2)}{48L}$$

$$M_C(x) = \frac{(L-x)(L^3\pi a^2\rho_t x + \rho_t ax\pi(ax - 4D_l)L^2 + x\pi(a^2x^2 - 4D_lax + 6D_l)\rho_t L - 48L_1F_1 - 48F_2L_2)}{48L} \quad (14)$$

From the bending moment, the bending stresses in the outer-fiber can be determined by dividing the bending moment by the section modulus

$$\sigma_{\text{outer},i}(x) = \frac{32M_i(x)}{(D_l - ax)^3\pi} \quad i = A, B, C \quad (15)$$

The ratio $a_F = F_1/F_2$ for which σ_{outer} is the same at L_1 and L_2 can be found by solving $\sigma_{\text{outer},A}(x = L_1) = \sigma_{\text{outer},B}(x = L_2)$ for a_F. The enclosed expression for this ratio is load dependent, and therefore is an implicit function. The force ratio as a function of F_1, for each individual pile, is shown in Fig. 25. With larger loads, the force ratio approaches an asymptotic value. For practical reasons, the choice was made to keep the force ratio constant during the tests. Because the piles were expected to fail at about a load of 10 kN, the force ratios were based on this value. The force ratios used are presented in Table 2.

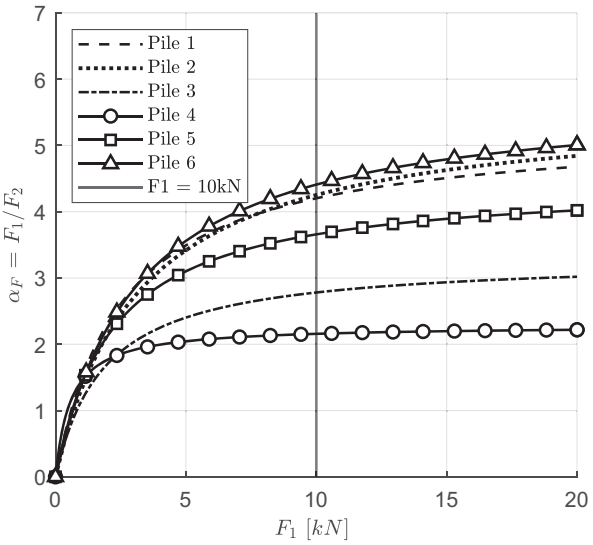

Fig. 25. Force ratio a_F as function of F_1 for all six piles.

Table 2. Force ratios for each individual pile during bending experiment

Pile no.	a_F
1	4.2
2	4.3
3	2.8
4	2.2
5	3.7
6	4.4

Appendix II. Derivation of Deflection from Curvature

To derive the deflection from the curvature profile $\kappa_t(x)$, a simply supported beam is considered in Fig. 26 (Hartsuijker 2001). The deflection y on location x can described by

$$y(x) = \varphi_a x - (x - x_1)\theta \quad (16)$$

where the rotation φ_a (rad) at Support A is described by Eq. (17); and θ (rad), the area of the integrated area between $x = 0$ and 'x' (Fig. 26, shaded area) is given by Eq. (18). The distance from A to the metric center of the integrated area between $x = 0$ and x is indicated by x_1, and can be determined using Eq. (19)

$$\varphi_a = \int_0^L \left(1 - \frac{x}{L}\right)\kappa_t(x)\text{dx} \quad (17)$$

$$\theta = \int_0^x \kappa_t(x)\text{dx} \quad (18)$$

$$x_1 = \frac{\int_0^x x\kappa_t(x)\text{dx}}{\int_0^x \kappa_t(x)\text{dx}} \quad (19)$$

Substituting Eqs. (17)–(19) into Eq. (16) results an expression for $y(x)$ which is dependent on $\kappa_t(x)$ and L. After simplifying, $y(x)$ can be described by

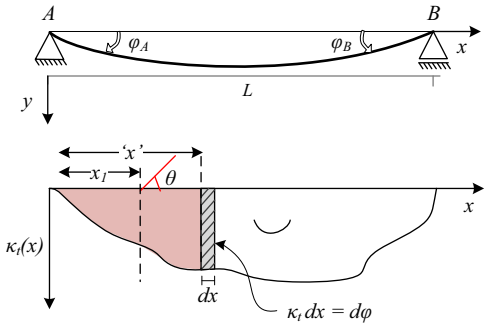

Fig. 26. Illustration of simply supported beam in bending with corresponding curvature diagram.

$$y(x) = -\frac{(\int_0^L (1-x)\kappa_t(x)dx)x - L(x(\int_0^x \kappa_t(x)dx) - (\int_0^x x\kappa_t(x)dx))}{L} \tag{20}$$

Appendix III. Derivation of Stress–Strain Relation

Mathematical expressions for the theoretical normalized moment–curvature of a circular cross section is presented in Eq. (21), where $\sin(a^*) = 1/\kappa^*$ (Pandit and Patel 2022)

$$M^* = \frac{16}{3\pi}\left(1 - \frac{1}{\kappa^{*2}}\right)^{3/2} + \frac{2\kappa^*}{\pi}\left(a^* - \frac{\sin(4a^*)}{2}\right) \tag{21}$$

where

$$a^* = \arcsin\left(\frac{1}{\kappa^*}\right) \tag{22}$$

$$\kappa^* = \frac{\kappa E_b h}{2\sigma} \tag{23}$$

Substituting Eqs. (22) and (23) into Eq. (21) and multiplying this by the first yield moment M_0 [Eq. (24)] results in an expression for the bending moment

$$M_0 = \frac{\pi h^3 \sigma}{32} \tag{24}$$

$$M = \frac{\left(\frac{16\left(1-\frac{4\sigma^2}{\kappa^2 E_b^2 h^2}\right)^{\frac{3}{2}}}{3\pi} + \frac{\kappa E_b h\left(\arcsin\left(\frac{2\sigma}{\kappa E_b h}\right) - \frac{\sin\left(4\arcsin\left(\frac{2\sigma}{\kappa E_b h}\right)\right)}{4}\right)}{\sigma\pi}\right)\pi h^3 \sigma}{32} \tag{25}$$

Substitution of the curvature κ with $2\varepsilon/h$ and simplification of Eq. (25) results in an expression for the bending moment as function of E_b, h, ε and σ

$$M = \frac{h^3\left(\left(\frac{8}{3}E_b^2\varepsilon^2\sigma - \frac{8}{3}\sigma^3\right)\sqrt{\frac{E_b^2\varepsilon^2 - \sigma^2}{E_b^2\varepsilon^2}} + E_b^3\varepsilon^3\left(\arcsin\left(\frac{\sigma}{E_b\varepsilon}\right) - \frac{\sin\left(4\arcsin\left(\frac{\sigma}{E_b\varepsilon}\right)\right)}{4}\right)\right)}{16E_b^2\varepsilon^2} \tag{26}$$

where M = bending moment computed from load cell measurements, which varies along the pile length. The modulus of elasticity (E_b) varies along the pile. Additionally, the strain (ε) is computed from the measured curvature (κ) and the measured effective pile diameter (h), both of which vary along the length of the pile. Furthermore, the maximal bending stress (σ), which also varies along the pile length, is the parameter to be computed.

Data Availability Statement

The data set used in this study was presented by Hemel et al. (2023).

Acknowledgments

The Delft University of Technology (DUT) conducted this research with valuable support and funding from the Municipality of Amsterdam (MA). The construction works for the experiments were carried out by De Klerk Werkendam (DKW), and the monitoring was conducted by IV-Infra (IV). The fiber optics were installed by Gemeente Rotterdam (GR). The full team for this study consisted of Dr. Mart-Jan Hemel, Dr. Dirk Jan Peters, Dr. Mandy Korff, Prof. Dr. Bas Jonkman (DUT), Erik Hutcheson (MA), Jelle van Ophuizen (IV), Ir. Erik Valckenier (IV), Ir. Willem van Bommel (GR), and Peter van Santen (DKW).

References

Aicher, S., and G. Stapf. 2016. "Compressive strength parallel to the fiber of spruce with high moisture content." *Eur. J. Wood Wood Prod.* 74 (4): 527–542. https://doi.org/10.1007/s00107-015-1004-z.

Amsterdam Gemeente. 1975. "Amsterdam op palen - de geschiedenis van het funderen." In *Maandblad van de Dienst der Publieke werken van Amsterdam, jaargang*, 25. Amsterdam, Netherlands: Dienst der Publieke Werken.

Björdal, C. G., and J. Elam. 2021. "Bacterial degradation of nine wooden foundation piles from Gothenburg historic city center and correlation to wood quality, environment, and time in service." *Int. Biodeterior. Biodegrad.* 164 (Jan): 105288. https://doi.org/10.1016/j.ibiod.2021.105288.

Buslov, V. M., and P. T. Scola. 1991. "Inspection and structural evaluation of timber pier: Case study." *J. Struct. Eng.* 117 (9): 2725–2741. https://doi.org/10.1061/(ASCE)0733-9445(1991)117:9(2725).

Ceccato, F. 2013. "Effect of wood degradation and soil creep on the behavior of wooden pile foundation in Venice." In *Proc., 5th Int. Young Geotechnical Engineers' Conf.* London: International Society for Soil Mechanics and Geotechnical Engineering.

Cerda, G., and R. W. Wolfe. 2003. "Bending strength of Chilean radiata pine poles." *For. Prod. J.* 53 (4): 61–65.

Chen, Y., and F. Lam. 2013. "Bending performance of box-based cross-laminated timber systems." *J. Struct. Eng.* 139 (12): 04013006. https://doi.org/10.1061/(ASCE)ST.1943-541X.0000786.

Chitchumnong, P., S. Brooks, and G. Stafford. 1989. "Comparison of three- and four-point flexural strength testing of denture-base polymers." *Dent. Mater.* 5 (1): 2–5. https://doi.org/10.1016/0109-5641(89)90082-1.

Christoforo, A. L., F. A. R. Lahr, E. A. M. Morales, A. L. Zangiácomo, and T. H. Panzera. 2012. "Influence of displacements on calculus of the longitudinal modulus of elasticity of *Pinus caribaea* structural round timber beams." *Int. J. Agric. For.* 2 (4): 157–160. https://doi.org/10.5923/j.ijaf.20120204.04.

Cline, M., and A. L. Heim. 1912. Vol. 108. of *Tests of structural timbers*. Washington, DC: USDA.

Cown, D., and J. Hutchison. 1983. "Wood density as an indicator of the bending properties of Pinus radiata poles." *N. Z. J. For. Sci.* 13 (1): 87.

Das, B. M. 2010. *Geotechnical engineering handbook*. Fort Lauderdale, FL: J. Ross Publishing.

Gard, W., and J. van de Kuilen. 2018. "Micro-drilling resistance measurements of dense hardwoods for hydraulic structures." In *Proc., WCTE-World Conf. on Timber Engineering*. Seoul: Korean Society of Wood Science and Technology.

Green, D. W., T. M. Gorman, J. W. Evans, and J. F. Murphy. 2006. "Mechanical grading of round timber beams." *J. Mater. Civ. Eng.* 18 (1): 1–10. https://doi.org/10.1061/(ASCE)0899-1561(2006)18:1(1).

Harmsen, L., and T. V. Nissen. 1965. "Timber decay caused by bacteria." *Nature* 206 (4981): 319. https://doi.org/10.1038/206319a0.

Hartsuijker, C. 2001. *Spanningen, vervormingen en verplaatsingen*. Hague, Netherlands: Academic Service.

Hemel, M.-J., M. Korff, and D. J. Peters. 2022. "Analytical model for laterally loaded pile groups in layered sloping soil." *Mar. Struct.* 84 (Jan): 103229. https://doi.org/10.1016/j.marstruc.2022.103229.

Hemel, M.-J., D. J. Peters, T. Schweckendiek, and S. N. Jonkman. 2024. "Reliability updating for lateral failure of historic quay walls." *Georisk: Assess. Manage. Risk Eng. Syst. Geohazards* 18 (4): 1–22. https://doi.org/10.1080/17499518.2024.2302141.

Hemel, M.-J., J. van Ophuizen, D. J. Peters, W. van Bommel, E. Valckenier, and A. den Dekker. 2023. *Four-point-bending experiments on historic quay wall foundation piles; Data underlying the dissertation: 'Amsterdam quays under pressure—Modelling and testing of historic canal walls'*. Delft, Netherlands: 4TU.ResearchData.

Huisman, D., E. Kretschmar, and N. Lamersdorf. 2008. "Characterising physicochemical sediment conditions at selected bacterial decayed wooden pile foundation sites in the Netherlands, Germany, and Italy." *Int. Biodeterior. Biodegrad.* 61 (1): 117–125. https://doi.org/10.1016/j.ibiod.2007.07.008.

Humar, M., A. Balzano, D. Kržišnik, and B. Lesar. 2021. "Assessment of wooden foundation piles after 125 years of service." *Forests* 12 (2): 143. https://doi.org/10.3390/f12020143.

Ido, H., H. Nagao, H. Kato, and S. Miura. 2013. "Strength properties and effect of moisture content on the bending and compressive strength parallel to the grain of sugi (*Cryptomeria japonica*) round timber." *J. Wood Sci.* 59 (1): 67–72. https://doi.org/10.1007/s10086-012-1297-z.

Kemper, A. R., C. McNally, C. A. Pullins, L. J. Freeman, S. M. Duma, and S. W. Rouhana. 2007. "The biomechanics of human ribs: Material and structural properties from dynamic tension and bending tests." SAE Technical Paper 2007-22-0011. Warrendale, PA: SAE International.

Klaassen, R. K. W. M. 2008. "Bacterial decay in wooden foundation piles—Patterns and causes: A study of historical pile foundations in the Netherlands." *Int. Biodeterior. Biodegrad.* 61 (1): 45–60. https://doi.org/10.1016/j.ibiod.2007.07.006.

Klaassen, R. K. W. M., and J. G. M. Creemers. 2012. "Wooden foundation piles and its underestimated relevance for cultural heritage." *J. Cult. Heritage* 13 (3): S123–S128. https://doi.org/10.1016/j.culher.2012.02.014.

Larson, D., R. Mirth, and R. Wolfe. 2004. "Evaluation of small-diameter ponderosa pine logs in bending." *For. Prod. J.* 54 (12): 52–58.

Lim, J., J.-K. Oh, H. Yeo, and J.-J. Lee. 2013. "Behavior of center-bored round timber beams in center-point bending test." *J. Wood Sci.* 59 (5): 389–395. https://doi.org/10.1007/s10086-013-1346-2.

Lopez-Anido, R., A. P. Michael, and T. C. Sandford. 2003. "Experimental characterization of FRP composite-wood pile structural response by bending tests." *Mar. Struct.* 16 (4): 257–274. https://doi.org/10.1016/S0951-8339(03)00021-2.

Morales-Conde, M. J., and J. S. Machado. 2017. "Evaluation of cross-sectional variation of timber bending modulus of elasticity by stress waves." *Constr. Build. Mater.* 134 (Jan): 617–625. https://doi.org/10.1016/j.conbuildmat.2016.12.188.

NEN. 2016. *Structural timber—Strength classes*. NEN-EN 338:2016. Delft, Netherlands: Nederlands Normalisatie Instituut.

Pagella, G., M. Mirra, G. Ravenshorst, and J. van de Kuilen. 2022a. "Influence of knots and density distribution on compressive strength of wooden foundation piles." In *Current perspectives and new directions in mechanics, modelling and design of structural systems*, 1689–1695. Boca Raton, FL: CRC Press.

Pagella, G., G. Ravenshorst, W. Gard, and J. W. van de Kuilen. 2022b. "Characterization and assessment of the mechanical properties of spruce foundation piles retrieved from bridges in Amsterdam." In *Proc., 4th Int. Conf. on Timber Bridges*. Rotterdam, Netherlands: International Council for Research and Innovation in Building and Construction.

Pais, J. C., and J. Harvey. 2012. *Four point bending*. Boca Raton, FL: CRC Press.

Pandit, D., and B. N. Patel. 2022. "On numerical moment-curvature relationship of a beam." *Sādhanā* 47 (1): 1–9. https://doi.org/10.1007/s12046-021-01782-2.

Ranta-Maunus, A., J. K. Denzler, and P. Stapel. 2011. *Strength of European timber: Part 2. Properties of spruce and pine tested in Gradewood project*. Espoo, Finland: VTT Technical Research Centre of Finland.

Thurston, R. H. 1879. "On the strength of American timber." *J. Franklin Inst.* 108 (4): 217–235. https://doi.org/10.1016/0016-0032(79)90282-5.

van Casteren, A., W. Sellers, S. Thorpe, S. Coward, R. Crompton, and A. Ennos. 2012. "Why don't branches snap? The mechanics of bending failure in three temperate angiosperm trees." *Trees* 26 (3): 789–797. https://doi.org/10.1007/s00468-011-0650-y.

van de Kuilen, J. W., O. Beketova-Hummel, G. Pagella, G. Ravenshorst, and W. Gard. 2021. "An integral approach for the assessment of timber pile foundations." In *Proc., World Conf. on Timber Engineering 2021, WCTE 2021*. Rotterdam, Netherlands: International Council for Research and Innovation in Building and Construction.

van Tussenbroek, G. 2012. "Historisch hout in Amsterdamse monumenten." In *Dendrochronologie–houthandel–toepassing*. Amsterdam, Netherlands: Stichting Historisch Hout.

Varossieau, W. 1949. *Opgegraven en aangetast hout uit biologisch oogpunt bezien*. Hague, Netherlands: Netherlands Organization for Applied Scientific Research.

Wang, L., and B. Young. 2016. "Behavior of cold-formed steel built-up sections with intermediate stiffeners under bending. I: Tests and numerical validation." *J. Struct. Eng.* 142 (3): 04015150. https://doi.org/10.1061/(ASCE)ST.1943-541X.0001428.

Wilkinson, T. L. 1968. Vol. 101 of *Strength evaluation of round timber piles*. Madison, WI: Forest Products Laboratory.

Winsen, M. V., H. Velzen, M. Dasselaar, and A. van der Mark. 2015. "Archeologisch en bouwhistorisch bureauonderzoek van de historische binnenstad van Gouda–In het kader van het projectplan "stevige stad op slappe bodem." In *FlexusAWC/ArcheoMedia Bv. Archeologisch en cultuurhistorisch bureauonderzoek*, 50. Gouda, Netherlands: FlexusAWC/ArcheoMedia Bv.

Wolfe, R., and J. Murphy. 2005. "Strength of small-diameter round and tapered bending members." *For. Prod. J.* 55 (3): 50–55.

Yin, Y., Y. Qiao, and S. Hu. 2019. "Four-point bending tests for the fracture properties of concrete." *Eng. Fract. Mech.* 211 (Jun): 371–381. https://doi.org/10.1016/j.engfracmech.2019.03.004.